reinforcement elongates, the fans open and the cracks between the struts widen similarly to the critical diagonal crack. Due to the elongation of the reinforcement, this deformation pattern can be associated with flexure while the bottom deformation pattern in Fig. 2a is associated with shear.

In the shear pattern the fans remain undeformed and the deformations concentrate along the critical diagonal crack. The displacement in the crack equals DOF Δ_c and causes significant shear distortions at both ends of the crack. At the top end the CLZ develops high diagonal compressive stress while at the bottom end the longitudinal reinforcement is subjected to double curvature. As it will be shown later, the diagonal compression in the CLZ has a significant contribution to the shear resistance of the beam. As hinted in Fig. 2a, the size of the CLZ is determined by a characteristic length l_{b1e} while the length over which the bottom reinforcement bends is l_k.

Lengths l_{b1e} and l_k as well as the rest of the geometrical properties of the kinematic model are expressed with Eqs. 1-4 in Fig. 2b. The expressions for l_k, the angle of the critical crack α_1, and the cracked length along the longitudinal reinforcement l_t have been adopted directly from the kinematic model for deep beams[11], while the characteristic length of the CLZ l_{b1e} requires a different expression. In deep beams l_{b1e} is proportional to the width of the column/plate loading the beam (see Fig. 1c), while in coupling beams this length is not clearly defined due to the large dimensions of the adjacent shear walls. A similar situation arises in the base of short shear walls where the CLZ of the wall merges into a large foundation. Recent studies on shear walls[13] have shown that l_{b1e} can be estimated reasonably well as a percentage of the diagonal of the wall $\sqrt{a^2+h^2}$, and therefore the same expression is adopted here for coupling beams (Eq. 1).

Having formulated the kinematics of short coupling beams, the kinematic model is used to express the deformations of the shear span as functions of DOFs $\varepsilon_{t,avg}$ and Δ_c, see Fig. 2c. These equations were derived based on small-displacements kinematics[10,14]. Equations 5-8 express the complete displacement field of the beam in an x-z coordinate system attached to the right end section. In these equations the horizontal and vertical displacements of each point from the shear span are obtained as a superposition of two terms, one due to $\varepsilon_{t,avg}$ and the other due to Δ_c. The displacement field equations are in turn used to derive expressions for some important deformations along the critical diagonal crack, i.e. the strain in the stirrups halfway along the crack ε_v as well as the crack displacements at the same location (crack width w and slip s), see Eq. 9-11. These deformations are again functions of the two DOFs of the kinematic model. The stirrup strain and crack displacements will be used in the following section to evaluate the mechanisms of shear resistance across the critical diagonal crack. Once the shear mechanisms are expressed with $\varepsilon_{t,avg}$ and Δ_c, the values of the DOFs of the kinematic model and the complete behavior of the beam will be obtained by establishing the equilibrium of the forces in the beam.

(a) Deformation patterns and DOFs

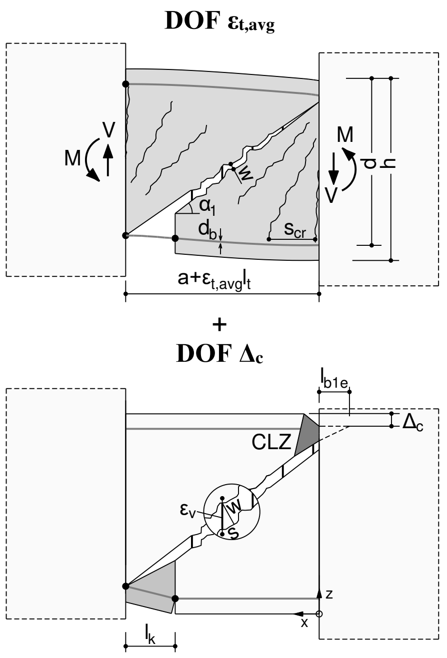

(b) Geometry

Characteristic length of critical loading zone

(1) $l_{b1e} = 0.11\sqrt{a^2+h^2}$

Angle of critical crack

(2) $\alpha_1 \approx \alpha \geq 35^\circ$

$\alpha = \operatorname{atan}\left(\frac{h}{a}\right)$

Dowel length

(3) $l_k = l_0 + d(\cot\alpha - \cot\alpha_1)$

$l_0 = 1.5(h-d)\cot\alpha_1 \geq s_{cr}$

$s_{cr} = \frac{0.28 d_b}{\rho_l}\frac{2.5(h-d)}{d}$

Cracked length along longitudinal reinforcement

(4) $l_t = d\cot\alpha_1 + l_k - l_0$

(c) Deformations

Displacement field

- below critical crack

(5) $\delta_x = \varepsilon_{t,avg}x$

(6) $\delta_z = \frac{\varepsilon_{t,avg}x^2}{h-z}$

- above critical crack

(7) $\delta_x = \varepsilon_{t,avg}\left(h\cot\alpha + x - a\right)$

(8) $\delta_z = \Delta_c + \frac{az\cot\alpha - (x-a)^2}{z}\varepsilon_{t,avg}$

Stirrup strain

(9) $\varepsilon_v = 2\frac{\Delta_c + 0.25\varepsilon_{t,avg}d\cot^2\alpha_1}{0.9d}$

Crack width and slip

(10) $w = \frac{\varepsilon_{t,avg}l_k}{2\sin\alpha_1} + \Delta_c\cos\alpha_1$

(11) $s = \Delta_c\sin\alpha_1$

Fig. 2 — Two-parameter kinematic model for short coupling beams.

MECHANISMS OF SHEAR RESISTANCE IN SHORT REINFORCED CONCRETE BEAMS

The deformations described by the kinematic model indicate the presence of at least four mechanisms of shear resistance in short coupling beams. These mechanisms are shown in the free-body diagram in Fig. 3. In addition to the shear carried in the critical loading zone V_{CLZ}, the other mechanism include the tension in the stirrups V_s, the aggregate interlock across the critical diagonal crack V_{ci}, and the dowel action of the longitudinal reinforcement V_d. Shear components V_{CLZ} and V_d are associated with the transverse displacement Δ_c, V_s with strain ε_v, and V_{ci} with the crack displacements w and s. The goal of this section is to express the shear forces with the corresponding deformations, and ultimately with the DOFs of the kinematic model via compatibility equations 9-11. Much of these derivations have been presented elsewhere for deep beams[15] and the results are summarized here with some modifications.

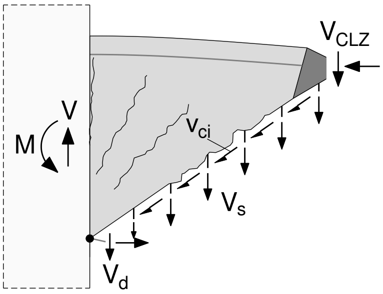

Fig. 3 — Shear mechanisms in short RC coupling beams.

Critical loading zone

In the critical loading zone the shear is resisted by diagonal compressive stresses inclined at angle α (Eq. 2). These stresses σ are shown in Fig. 4 on the deformed configuration of the CLZ. It has been shown elsewhere[10] that the shape of the CLZ prior to deformations can be approximated with a triangle with two equal sides of $1.5l_{b1e}$ (top and left) and equal angles α adjacent to these sides. Under loading the bottom inclined side of the CLZ shortens with a strain ε_{max}, while the length of the two equal sides remains unchanged. Based on this local kinematics, strain ε_{max} is expressed with DOF Δ_c as shown in Fig 4., and stresses σ are expressed with ε_{max} by using appropriate stress-strain relationships for the concrete in uniaxial compression[16]:

$$\sigma = \frac{n\left(\varepsilon/\varepsilon_c^{'}\right)}{n-1+\left(\varepsilon/\varepsilon_c^{'}\right)^{nk}} f_c^{'} \tag{12}$$

where $$n = 0.8 + \frac{f_c^{'}}{17} \text{ MPa (1 MPa = 145 psi)}$$

$$k = 0.67 + \frac{f_c^{'}}{62} \text{ MPa}$$

$$E_c = 3320\sqrt{f_c^{'}} + 6900 \text{ MPa}$$

$$\varepsilon_c^{'} = \frac{f_c^{'}}{E_c}\frac{n}{n-1}$$

The shear force carried by the critical loading zone is determined by integrating the concrete stresses σ and by taking into account the triangle of forces in Fig. 4:

$$V_{CLZ} = k_c \sigma_{avg}\left[\varepsilon_{max}\left(\Delta_c\right)\right] b l_{b1e} \sin^2\alpha \tag{13}$$

where σ_{avg} is the average stress in the CLZ and b is the width of the beam section. The average stress is obtained by calculating the area under the σ-ε curve from zero strain up until ε_{max}, and by dividing the result by ε_{max}. The additional coefficient in Eq. 13 k_c takes into account the compression softening effect in the CLZ caused by the tensile strain $\varepsilon_{t,avg}$ in the top longitudinal reinforcement[17]:

$$k_c = 1/\left(0.8 + 170\varepsilon_1\right) \le 1 \tag{14}$$

where ε_1 is the principal tensile strain in the CLZ estimated as

$$\varepsilon_1 = 0.75\varepsilon_{t,avg}\left(1+\cot^2\alpha\right) \tag{15}$$

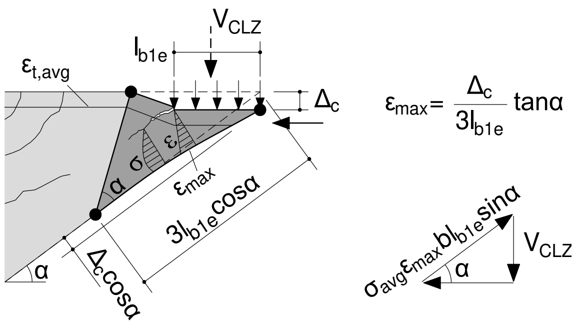

Fig. 4 — Modelling of the critical loading zone (CLZ).

Aggregate interlock

As mentioned earlier, the aggregate interlock stresses across the critical diagonal crack v_{ci} depend on the width and slip displacements in the crack. To simplify the calculations, these displacements are calculated only halfway along the crack. As evident from Eq. 10-11, the crack width w depends on both DOFs of the kinematic model, while the slip s depends only on DOF Δ_c. Based on equilibrium, the shear force resisted by aggregate interlock V_{ci} is expressed as:

$$V_{ci} = v_{ci}\left(w,s\right)bd \tag{16}$$

where the shear stress $v_{ci}(w,s)$ is calculated based on a modified version of the contact density model proposed by Li et al.[18]:

$$v_{ci} = 0.115\int_{-\frac{\pi}{2}}^{\frac{\pi}{2}} \sigma_{con} K \sin\varphi\cos\varphi d\varphi \text{, MPa (1 MPa = 145 psi)} \tag{17}$$

$$\sigma_{con} = 13.7\sqrt[3]{f_c'}\,\frac{s\sin\varphi - w\cos\varphi}{0.04}\begin{cases}\le 13.7\sqrt[3]{f_c'} \\ \ge 0\end{cases}\text{, MPa}$$

$$K = 1-\exp\left(1-\frac{a_g}{w}\right)\ge 0$$

where a_g is the maximum aggregate size and the crack displacements are inserted in mm (1 mm = 0.0394 in.). The integral in Eq. 17 is evaluated numerically by dividing the interval $-\pi/2\le\varphi\le\pi/2$ into a sufficient number of subintervals (~100).

Tension in the transverse reinforcement (stirrups)

The strain in the stirrups ε_v halfway along the critical crack is calculated from Eq. 9 as a function of DOFs $\varepsilon_{t,avg}$ and Δ_c. This strain is used together with a simple elastic – perfectly plastic stress-strain relationship for the steel to determine the stress in the stirrups. However, because the stirrup strains vary along the crack from maximum in the middle of the crack to nearly zero at the ends, an average stirrup stress $\sigma_{v,avg}$ is used for the calculation of V_s:

$$V_s = \sigma_{v,avg}\rho_v b\left(0.9d\right) \tag{18}$$

where $\rho_v \le 0.15f_c'/f_{yv}$ is the stirrup ratio and f_{yv} is the yield stress of the steel. The average stirrup stress is evaluated as a function of ε_v as follows:

$$\sigma_{v,avg} = \begin{cases} E_s\varepsilon_v/2 & when\ \varepsilon_v \le \varepsilon_{yv} \\ \dfrac{f_{yv}\varepsilon_{yv}/2 + f_{yv}\left(\varepsilon_v - \varepsilon_{yv}\right)}{\varepsilon_v} & when\ \varepsilon_v > \varepsilon_{yv}\end{cases} \tag{19}$$

where $\varepsilon_{vy}=f_{yv}/E_s$ is the yield strain of the stirrups and E_s is the modulus of elasticity.

Dowel action of the longitudinal reinforcement

The dowel action of the longitudinal reinforcement is associated with the bending of the bars along the length l_k, see Fig. 2a. To simplify the derivations, it is assumed that the bars are subjected to symmetrical double-curvature bending under an imposed transverse displacement Δ_c. Under these conditions it can be easily shown from beam theory that the shear force in the dowels is

$$V_d = n_b \frac{12 E_s \pi d_b^4}{64 l_k^3} \Delta_c \le n_b f_y \frac{d_b^3}{3 l_k} \left[1 - \left(\frac{\varepsilon_{t,avg}}{\varepsilon_y} \right)^2 \right] \tag{20}$$

where n_b is the number of bars (dowels), d_b is the bar diameter, f_y is the yield stress of the longitudinal reinforcement, and $\varepsilon_y=f_y/E_s$ is the yield strain of the reinforcement. The first term of this equation represents the initial linear elastic behavior of the bar-dowels, while the upper bound on this term accounts for the formation of plastic hinges at the ends of the dowels. Because simultaneously with Δ_c the bars are also subjected to longitudinal tension, the moment capacity of the plastic hinges is reduced by the expression in the square brackets which should not be taken smaller than zero. If strain $\varepsilon_{t,avg}$ exceeds the yield strain ε_y, the bars are yielding in tension and do not possess resistance in bending (V_d=0).

EQUILIBRIUM OF SHEAR FORCES AND PREDICTED BEAM BEHAVIOR

In addition to the kinematic conditions and constitutive relationships discussed in the previous two sections, it is also necessary to consider the equilibrium of the forces in short coupling beams. The vertical equilibrium of the top part of the beam in Fig. 3 requires that the shear force applied on the beam is equal to the sum of the shear components derived in the previous section. At the same time, the shear force can also be expressed from the moment equilibrium of one-half of the shear span as a function of the tension force T in the longitudinal reinforcement in the end section. As the two shear forces must be equal, the two main equilibrium conditions that need to be satisfied are:

$$V = V_{CLZ} + V_{ci} + V_s + V_d = 2Tz/a \tag{21}$$

where $z \approx 0.9d$ is the lever arm of the longitudinal forces in the end sections and a is the shear span. These equilibrium conditions, combined with the previously derived expressions for the shear components, will be used to predict the DOFs of the kinematic model and the complete behavior of short coupling beams. As components V_{CLZ}, V_{ci}, V_s, and V_d were expressed with the two DOFs of the kinematic model, it is also necessary to express the tensile force in the reinforcement with the average strain in the reinforcement (DOF $\varepsilon_{t,avg}$). The proposed expression for the relationship $T(\varepsilon_{t,avg})$ is

$$T = E_s A_s \varepsilon_{t,avg} + \frac{0.33\sqrt{f_c}}{\sqrt{1+200\varepsilon_{t,avg}}} A_{c,eff} \tag{22}$$

where the first term models the elastic behavior of bare reinforcement and the second term is the tension stiffening effect of the concrete around the reinforcement[17]. The concrete contributing to the tension stiffening effect has an area $A_{c,eff}$ estimated as the minimum of 2.5(h-d)b and hb/2[19].

With the expression for T, Eq. 21 will be used to determine DOF $\varepsilon_{t,avg}$ at different levels of loading up to failure, and in the post-peak regime of the coupling beam. Because the model is developed for shear critical beams, it is expected that DOF Δ_c increases monotonically throughout the loading. Owing to that, the analysis will be performed under controlled Δ_c.

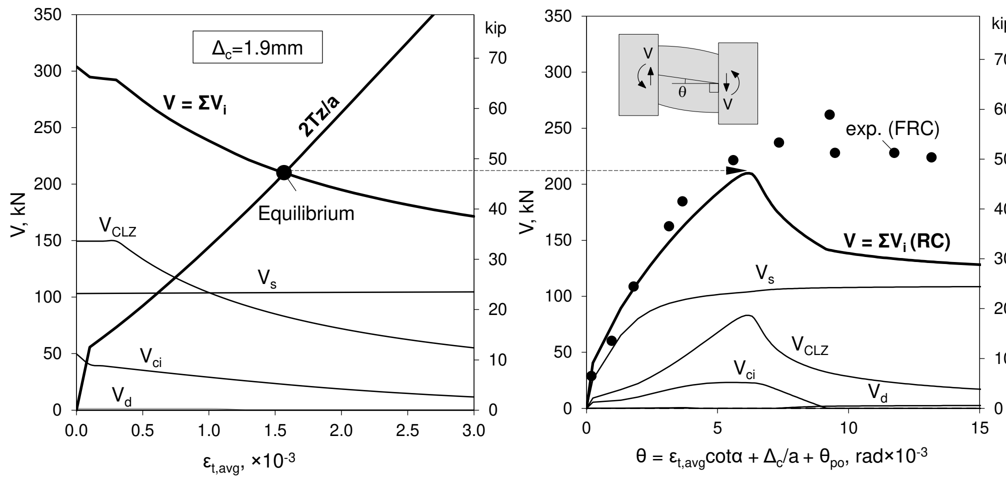

(a) Equilibrium of forces for a selected Δ_c (b) Complete load-displacement response

Fig. 5 — Solution procedure.

The solution of Eq. 21 for a selected value of Δ_c is illustrated graphically in Fig. 5a for a sample coupling beam (a/d=2.32, d=345 mm [13.58 in], f_c'=80.7 MPa [11700 psi], ρ_l=1.21%, and ρ_v=0.56%). On the horizontal axis of the plot is the unknown DOF $\varepsilon_{t,avg}$ while on the vertical axis are the shear forces. The descending thick curve corresponds to the sum of shear components V_{CLZ}, V_{ci}, V_s and V_d, while the ascending thick line represents 2Tz/a. Therefore, the solution of Eq. 21 lies at the intersection of the two lines where the shear forces are in equilibrium. More precisely, the abscissa of this point is the predicted value of DOF $\varepsilon_{t,avg}$ while the ordinate is the shear force on the beam for the selected value of Δ_c. The intersection point can be obtained most efficiently by using an iterative solution procedure based on the method of bisection.

Figure 5a also shows the individual shear components V_{CLZ}, V_{ci}, V_s and V_d, and how they vary with increasing $\varepsilon_{t,avg}$. The largest shear contribution in this case comes from the transverse reinforcement, and remains nearly constant along the whole range of strain values (curve V_s). The reason for this constant trend is that, while $\varepsilon_{t,avg}$ increases the strain in the stirrups, the selected value of Δ_c alone is sufficient to yield the steel (Eq. 9), and therefore V_s is equal to the yield force of the transverse reinforcement crossing the critical crack. Differently from component V_s, the shear carried in the critical loading zone V_{CLZ} exhibits a significant decline when the strain $\varepsilon_{t,avg}$ increases. This so-called strain effect in shear is due to the compression softening of the concrete in the CLZ expressed with the factor k_c in Eq. 13. A strain effect is also observed in the aggregate interlock and dowel action components V_{ci} and V_d. As $\varepsilon_{t,avg}$ increases, the width of the critical crack increases (Eq. 10), and the interlocking of the crack faces diminishes. Similarly, increasing $\varepsilon_{t,avg}$ results in reduced plastic moment capacity of the longitudinal reinforcement, and therefore reduced dowel action (Eq. 20).

Having obtained V and $\varepsilon_{t,avg}$ for a selected value of Δ_c, it is necessary to determine the global deformation of the beam in terms of chord rotation θ. Because equations 5-8 express the complete displacement field of the shear span, they can be used to derive the chord rotation as a function of the known DOFs of the kinematic model. More precisely, θ can be expressed from Eq. 8 by substituting x=a:

$$\theta = \delta_z(x=a)/a = \varepsilon_{t,avg}\cot\alpha + \Delta_c + \theta_{po} \tag{23}$$

The additional term θ_{po} in this equation is included to capture the increase of chord rotation caused by the strain penetration in the adjacent walls. As the longitudinal reinforcement is anchored in the walls, the strains along the reinforcement result in a pullout displacement in the end sections of the beam, and therefore an additional rotation about the neutral axis of these sections. Term θ_{po} is thus expressed with the pullout displacement δ_{po} as follows

$$\theta_{po} = \delta_{po}/(0.8d) \tag{24}$$

where 0.8d is the estimated distance from the tension reinforcement to the neutral axis in the end sections.

Displacement δ_{po} is evaluated as a function of the already calculated strains $\varepsilon_{t,avg}$ in the reinforcement in the shear span by using a model proposed by Sigrist[20]. In this model the anchorage length of the reinforcement is divided into two parts: l_1 near the edge of the wall where the reinforcement may yield, and l_2 farther in the wall where the reinforcement is elastic. The bond stress between the bar and the concrete is assumed constant in each zone with values of f_{ct} within l_1 and $2f_{ct}$ within l_2, where $f_{ct} = 0.3(f_c')^{2/3}$ (MPa) is the tensile strength of the concrete. Considering also the equilibrium of the bar, the following expressions are derived for the pullout displacement:

$$\delta_{po} = \frac{1}{2}\left(\varepsilon_{t,avg} + \frac{f_y}{E_s}\right)l_1 + \frac{1}{2}\min\left(\varepsilon_{t,avg}, \frac{f_y}{E_s}\right)l_2 \tag{25}$$

$$l_1 = \max\left(\sigma_{t,avg} - f_y, 0\right)\frac{d_b}{4f_{ct}}$$

$$l_2 = \min\left(\sigma_{t,avg}, f_y\right)\frac{d_b}{8f_{ct}}$$

where $\sigma_{t,avg}$ is the stress in the bar obtained from the strain $\varepsilon_{t,avg}$ by using a bi-linear stress-strain relationship with strain hardening. If $\sigma_{t,avg}$ is smaller than the yield strength of the steel f_y, length l_1 is zero and the pullout displacement is given only by the second term of Eq. 25.

Finally, the plots in Fig. 5a and 5b illustrate the calculation procedure to obtain the complete shear force vs. chord rotation response of short RC coupling beams. The calculations illustrated in Fig. 5a are repeated for different values of Δ_c with increasing magnitude. In these calculations the 2Tz/a line remains the same while the shear resistance curve ΣV_i changes with Δ_c. Each intersection point obtained in the left diagram is used to obtain a corresponding point from the global V-θ response. It can be seen from Fig. 5b that the proposed model predicts the complete response of the coupling beam, including the post-peak regime corresponding to large values of DOF Δ_c and large sliding in the critical diagonal crack. It is also noted that, for the selected beam, the chord rotation due to bar pullout represents a significant portion of the total rotation (~12% at peak load).

In addition to the predicted response of the RC coupling beam, Fig. 5b also shows the measured response of a fiber-reinforced concrete beam with a 1% fiber volume ratio (beam CCB3-80-2-1FS tested by Cai et al.[8]).The two beams have identical properties, except that the predictions were obtained without taking into account the steel fibers. Therefore, the difference between the experimental and predicted V-θ responses in Fig. 5b must correspond to the effect of the fibers. It can be seen that the FRC beam exhibited a higher strength and better ductility than predicted for the RC beam. To capture these effects, the following section focuses on the additional mechanisms of shear resistance provided by steel fibers.

EFFECT OF STEEL FIBRES

To account for the effect of steel fibers in the concrete, it is necessary to model two phenomena which are characteristic of fiber-reinforced concrete. These include the tension in the fibers across the critical diagonal crack and the enhanced compression behavior of the critical loading zone. The modelling will be performed by using constitutive relationships from the literature which will be integrated in the framework of the kinematic approach.

Tension in the fibers across the critical diagonal crack

The most obvious effect of the fibers is the bridging of the critical diagonal crack. This tension behavior across cracks has been studied by a number of researchers and is demonstrated schematically in Fig. 6 adapted from Voo and Foster[21]. The tensile stress across the crack is divided into a component transferred directly between the crack faces (tension softening) and a component transferred through the fibers. However, because the kinematic approach assumes a fully cracked member, and because the tension transferred directly by the concrete vanishes at small crack widths, only the tension due to the fibers will be considered for the modelling of FRP coupling beams. This stress σ_f can be estimated by using a simplified diverse embedment model (SDEM) proposed by Lee et al.[22] based on an earlier model by Voo and Foster[21]. The SDEM uses the following general formulation for the stress σ_f:

$$\sigma_f = \sigma_{st} + \sigma_{eh} \tag{26}$$

where σ_{st} is the stress due to the bond resistance along the length of the fibers and σ_{eh} is the resistance against pullout of the fibers provided by end hooks (if present). Both these components are expressed as functions of the crack width *w*, however, the latter component is neglected here for the sake of simplicity. The adopted expression for σ_f is thus

$$\sigma_f = \alpha_f \rho_f K_{st} \tau_{f,\max} \frac{l_f}{d_f}\left(1-\frac{2w}{l_f}\right)^2 \text{, MPa (1 MPa = 145 psi)} \tag{27}$$

where

$$K_{st} = \begin{cases} \dfrac{\beta_f}{3}\dfrac{w}{s_f} & for\ w < s_f \\ 1-\sqrt{\dfrac{s_f}{w}}+\dfrac{\beta_f}{3}\sqrt{\dfrac{s_f}{w}} & for\ w \geq s_f \end{cases}$$

where α_f=0.5 is a fiber orientation factor, ρ_f is the volumetric ratio of steel fibers in the concrete, l_f is the fiber length, d_f is the fiber diameter, $\tau_{f,max} = 0.396\sqrt{f_c'}$ (MPa) is the bond stress between the fibers and the concrete, β_f=0.67, and s_f=0.01 mm [0.39×10^{-3} in.] .

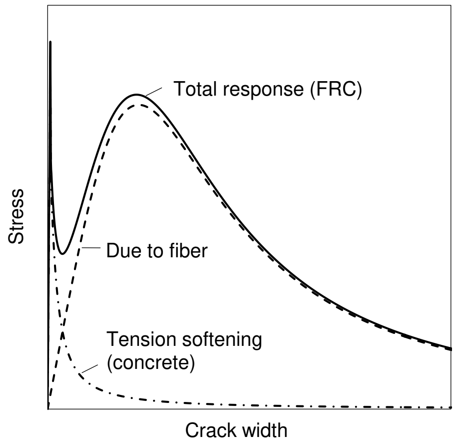

Fig. 6 — Tensile behavior of FRC vs. normal concrete (adapted from Voo and Foster, 2003[21]).

However, while the above equations were derived for cracks that exhibit pure opening, the critical diagonal crack in short coupling beams undergoes both opening and slip displacements. More precisely, the displacement in the cracks is predominantly in the vertical direction due to the relatively large contribution of DOF Δ_c. Therefore, stress σ_f will not evaluated as a function of *w*, but as a function of the vertical displacement in the crack w_v expressed with the DOFs of the kinematic model:

$$w_v = \frac{1}{2}\varepsilon_{t,avg} l_k \cot\alpha_1 + \Delta_c \tag{28}$$

Having expressed the stress across the critical crack, the additional shear mechanism due to fibers is

$$V_f = \sigma_{f,avg}\left(w_v\right) bd \big/ \sin\alpha \tag{29}$$

where $\sigma_{f,avg}(w_v)$ is the average stress transferred by the fibers across the critical diagonal crack with area bd/sinα. The average stress is used here for the same reasons the average stress in the stirrups was used in the expression for V_s: the crack displacement expressed by Eq. 28 is the maximum value which occurs approximately halfway along the crack, while near the ends of the crack the displacement reduces to almost zero. At a given value of w_v, the averaging is performed by integrating the $\sigma_f(w_v)$ curve from zero up to w_v, and by dividing the result by w_v.

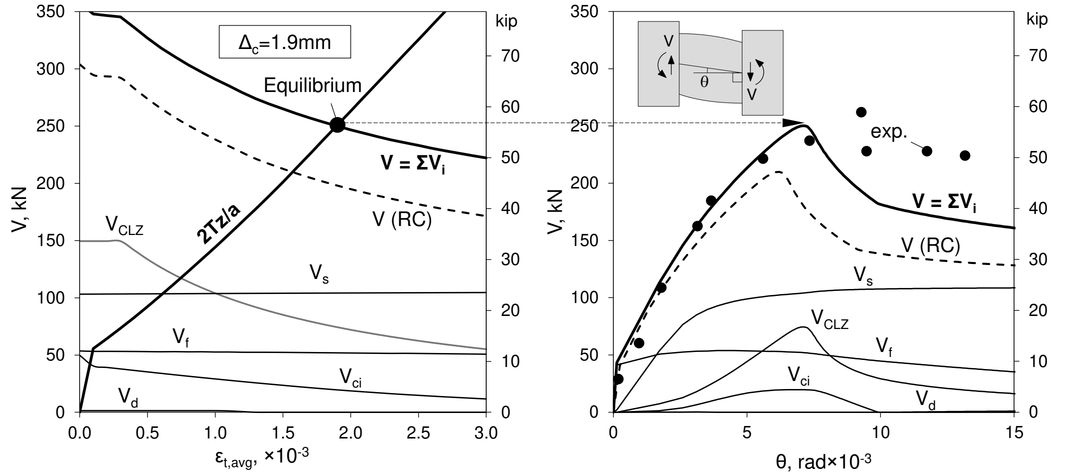

(a) Equilibrium of forces for a selected Δ_c (b) Complete load-displacement response

Fig. 7 — Effect of tension in the fibers across the critical diagonal crack.

Shear component V_f is added to components V_{CLZ}, V_{ci}, V_s and V_d to extend the model for short coupling beams. This is illustrated in Fig. 7 which is again generated for specimen CCB3-80-2-1FS in the same format as Fig 5. It can be seen from plot 7a that V_f is almost constant within the entire range of strains $\varepsilon_{t,avg}$. This is due to the dominant contribution of Δ_c to the vertical displacement in the critical crack (Δ_c=const in Fig. 7a). However, because Δ_c increases with increasing chord rotations, the shear contribution of the fibers eventually decreases in the global V-θ response (Fig. 7b). Nevertheless, for the selected beam with a 1% volumetric ratio of fibers, component V_f results in a significant increase of shear resistance (~19%). With this contribution, the kinematic approach captures well the pre-peak and peak response of the test specimen, while it can be seen that additional modifications are needed to better approximate the post-peak behavior.

Compressive behavior of the critical loading zone

In addition to bridging the critical diagonal crack, the steel fibers also affect the behavior of the critical loading zone. As discussed earlier, the concrete in this zone is subjected to diagonal compressive stresses, and the behavior of the zone can be described based on a stress-strain model for the concrete under uniaxial loading. However, while the stress-strain relationship given by Eq. 12 is appropriate for plain concrete, a different model is needed for fiber-reinforced concrete.

A number of researchers have studied the uniaxial compression behavior of FRC and have proposed stress-strain relationships. In order to ensure a smooth transition from reinforced concrete to FRC members, this paper focuses on a model by Ou et al.[23] that provides very similar results to those obtained with Eq. 12 when the fiber volume ratio is zero. Based on this model, the compressive stresses in FRC are expressed with the strains as follows:

$$\sigma = f'_{cf}\frac{\beta\left(\dfrac{\varepsilon}{\varepsilon'_{cf}}\right)}{\beta - 1 + \left(\dfrac{\varepsilon}{\varepsilon'_{cf}}\right)^{\beta}} \tag{30}$$

$$\varepsilon'_{cf} = \varepsilon_{c0} + 0.0007\left(RI_v\right)$$

$$\beta = 0.71\left(RI_v\right)^2 - 2\left(RI_v\right) + 3.05$$

$$f_{cf}^{'} = f_c^{'} + 2.35\left(RI_v\right)$$

where index $RI_v=\rho_f l_f/d_f$ accounts for the volumetric and aspect ratios of the fibers. One limitation of this model is that it applies only to normal-strength concrete with $f_c' \leq 60$ MPa [8702 psi], and therefore a model proposed Mansour et al.[24] is adopted for high-strength concrete. The equations of this model are not presented here for the sake of brevity.

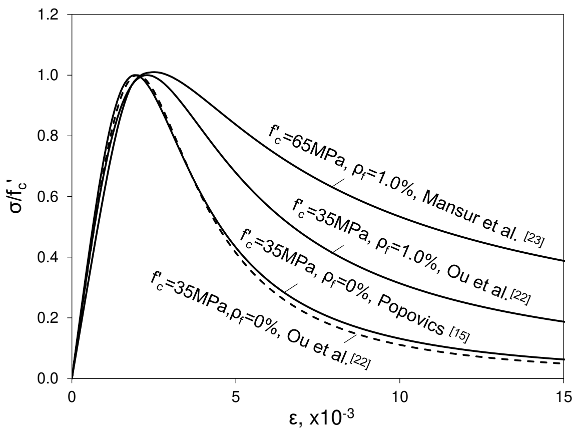

Fig. 8 — Compressive behavior of FRC.

The two models are plotted in Fig. 8 for different concrete strengths and fiber volume ratios. It can be seen that, while the steel fibers have a negligible effect in the pre-peak and peak regime, they improve significantly the post-peak behavior of concrete in compression.

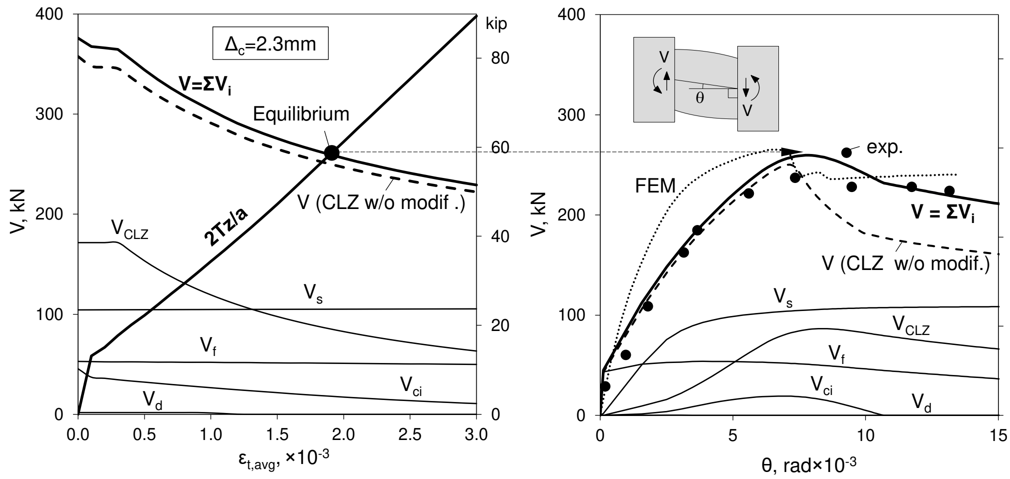

(a) Equilibrium of forces for a selected Δ_c (b) Complete load-displacement response

Fig. 9 — Effect of enhanced behavior of the critical loading zone.

These stress-strain relationships are included in the kinematic approach for coupling beams to modify the V_{CLZ} component of shear resistance. More precisely, Eq. 30 is used to recalculate the average concrete stresses σ_{avg} in Eq. 13 as a function of the maximum strain in the CLZ $\varepsilon_{max}(\Delta_c)$. With this modification, the model is applied once again to beam CCB3-80-2-1FS and the results are presented in Fig. 9. Plot 9b shows that, similarly to the stress-strain curves for FRC in compression, the fibers in the CLZ result in an enhanced post-peak behavior of the coupling beam. While in Fig. 7b shear component V_{CLZ} exhibits a brittle behavior, in Fig. 9b it maintains a nearly constant value after the beam reaches the peak load. It can also be seen that the extended kinematic approach captures very well the complete response of the test specimen both in the pre- and post- peak regimes. It should be noted that one such analysis requires a straightforward input without open parameters and negligible time for computations.

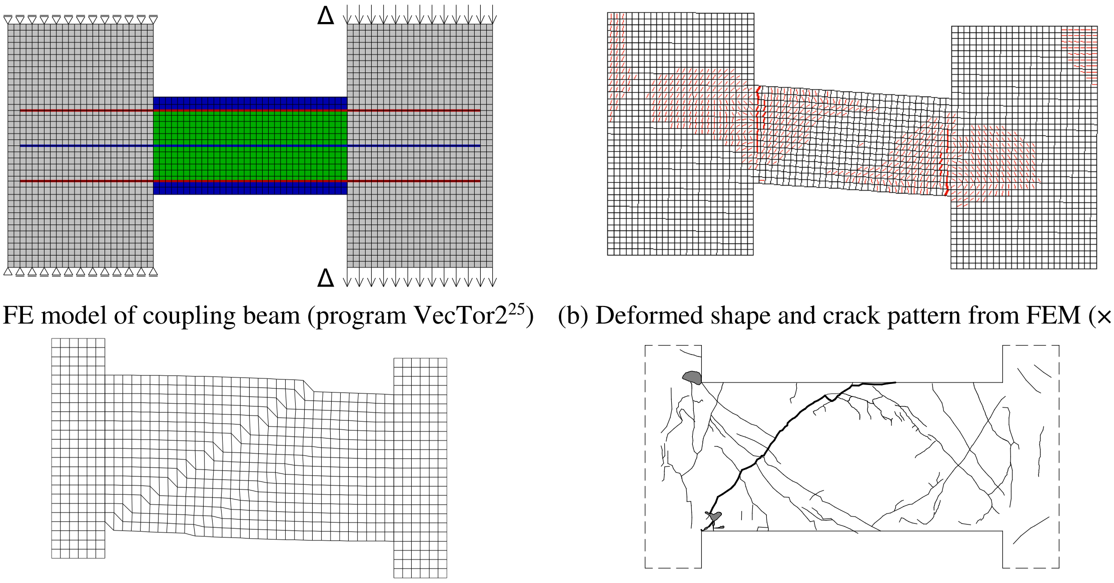

(a) FE model of coupling beam (program VecTor2[25]) (b) Deformed shape and crack pattern from FEM (×10)

(c) Deformed shape from kinematic approach (×10) (d) Crack diagram from test (adapted from Cai et al.[8])

Fig. 10 — Predicted and observed failure modes of beam CCB3-80-2-1FS[8]

COMPARISONS WITH TESTS AND FEM SIMULATIONS

To further evaluate the appropriateness of the proposed model, its predictions will be compared to other experimental results and to the predictions of a significantly more complex finite element model (FEM). The FE analyses are performed with program VecTor2 based on the Disturbed Stress Field Model (DSFM[25]). The DSFM is a smeared rotating crack model that originates from the Modified Compression Field Theory for reinforced concrete elements subjected to shear[25]. In the DSFM, the cracks are assumed parallel to the principal compressive stress directions in the concrete, while the principal strain directions deviate from the stress directions due to slip displacements in the cracks. The slip displacements and crack widths are used to calculate aggregate interlock stresses transferred across the cracks. In addition to aggregate interlock, the DSFM also accounts for the tension stiffening and softening of the concrete, compression softening and confinement of the concrete, as well as the yielding of the reinforcement. This formulation has been recently extended to also account for the effect of steel fibers based on the divers embedment model[26,27]. To ensure that the analyses can be reproduced easily, these effects were modelled based on the default advanced relationships implemented in VecTor2 with a few exceptions specific to FRC. The compression behavior of the concrete is modelled based on expressions proposed by Lee et al.[27] and the compression softening based on Vecchio[28].

Fig. 10a shows the finite element model of beam CCB3-80-2-1FS. The model consists of quadrilateral plane-stress elements for the FRC and truss elements for the top and bottom longitudinal reinforcement. Bond elements were introduced between the quadrilateral and truss elements to capture the bar pullout displacements. Since the stirrups were densely spaced, they were represented as smeared vertical reinforcement in the quadrilateral elements. The top and bottom concrete cover of the longitudinal reinforcement in the shear span was modelled with FRC elements without stirrups. The shear force and bending moments were introduced in the shear span via heavily reinforced concrete blocks on each side of the beam. One of the blocks was clamped while the other was subjected to imposed vertical displacements along its top and bottom edges. Because the displacements are constant along the block, they restrain its rotation while allowing unrestrained horizontal movements as in the test. The displacements were increased monotonically to capture the entire behavior of the beam under symmetrical double-curvature bending, including the post-peak response.

The shear force vs. chord rotation response of beam CCB3-80-2-1FS produced by the FEM is plotted in Fig. 9b together with the experimental data and the predictions of the kinematic approach. It can be seen that the finite element model overestimates the pre-peak stiffness of the beam, but captures very well the measured peak and post-peak response.

The peak response of beam CCB3-80-2-1FS is illustrated in Fig. 10b-d with the help of deformation patterns and crack diagrams at failure. Plots 10b and 10c compare the predicted deformed shapes at failure produced by the FEM and the kinematic approach. The latter deformed shape is calculated from Eq. 5-8 with the predicted values of DOFs $\varepsilon_{t,avg}$ and Δ_c. It can be seen that both models predicted extensive shear cracking but different failure modes. While the kinematic approach predicts a shear failure along a critical crack inclined at 35°, the FEM predicts a flexural failure by yielding of the longitudinal reinforcement in the end sections. It is evident from Fig.

10d that the former failure mode is in better agreement with the crack pattern observed in test CCB3-80-2-1FS. According to this pattern, the beam failed in shear along a crack inclined at approximately 45°. It should be noted that, because the beam had a relatively large aspect ratio (a/h=2), the kinematic approach predicts two potentially critical cracks, one at each end of the shear span. However, even though the two cracks are under identical conditions, it is assumed that only one of them is critical and develops the shear displacement Δ_c.

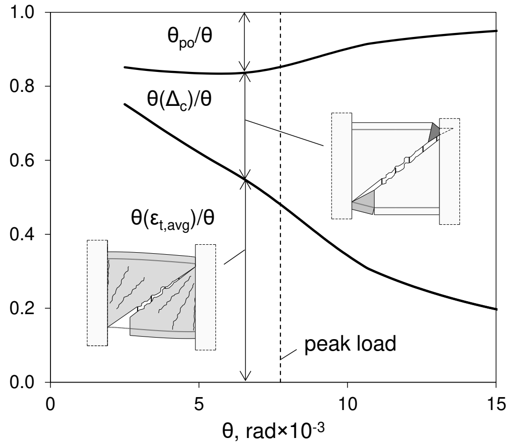

Fig. 11 — Predicted components of chord rotation according to the kinematic approach – specimen CCB3-80-2-1FS8[8]

Because the deformation pattern in Fig. 10c is obtained as a superposition of two deformation patterns associated with DOFs $\varepsilon_{t,avg}$ and Δ_c, it is of interest to study how these DOFs contribute to the global chord rotation of specimen CCB3-80-2-1FS. As discussed earlier, in addition to the two DOFs, the pullout of the longitudinal reinforcement from the adjacent walls is also included in the kinematic approach (Eq. 23). Fig. 11 shows how these three contributions vary with increasing chord rotations. The contributions are normalized with respect to the current rotation, and therefore add up to unity. It can be seen that initially the rotations are governed by DOF $\varepsilon_{t,avg}$ and the pullout deformations. Therefore, the beam behaves mainly according to the flexural deformation pattern of the kinematic approach with negligible slip displacements in the critical crack. However, as the chord rotations and the shear on the beam increase, the relative contribution of the flexural pattern decreases and that of the shear pattern governed by DOF Δ_c increases. At failure the contributions of DOFs $\varepsilon_{t,avg}$ and Δ_c are similar (48% and 37%), while the bar pullout is responsible for 15% of the chord rotation. Because the beam failed in shear, in the post-peak regime the deformations are dominated by Δ_c with corresponding large opening and sliding displacements along the critical crack. In contrast, because the FEM predicts flexural failure, the predominant contribution to the chord rotation according to this model comes from the strains in the longitudinal reinforcement in both the pre- and post- peak regimes.

In addition to specimen CCB3-80-2-1FS, the kinematic approach and FEM are also applied to 18 specimens from two experimental studies[8,9]. The properties of the specimens as well as their measured shear strengths are provided in Table 1. The a/d ratio of the beams varies from 1.11 to 2.32, the effective depth d from 345 mm to 360 mm [13.58 in. to 14.17 in.], the longitudinal reinforcement ratio ρ_l from 1.21% to 2.0%, the stirrup ratio ρ_v from 0% to 2%, the concrete compressive strength f_c' from 37.5 MPa to 80.7 MPa [5439 psi to 11705 psi], and the volumetric fiber ratio from 0 to 2%. The beams were subjected to either monotonic[9] or reversed cyclic loading[8]. The measured and predicted shear force vs. chord rotation responses of nine of the specimens are shown in Fig. 12. These beams were selected because the V-θ curves of the rest of the specimens were not reported. Overall, the kinematic approach captures the response well, particularly the peak response corresponding to diagonal tension failure. The model overestimates the pre-peak stiffness of four of the beams (CCB3-50-2-1FS, CCB3-50-2-1.5FS, S-10/M, and S-15/M) and underestimates the ductility of two test specimens (CCB3-50-2-1FS and CCB3-50-2-1.5FS). With regards to the stiffness, it should be noted that some inconsistencies are also observed in the test data. Specimen S-15/M for example, which had an a/d ratio of 1.5, had a significantly lower stiffness than the companion test S-20/M which was significantly more slender (a/d=2.0). As with regards to the FEM predictions, they agree reasonably well with those of the kinematic approach in the pre-peak and peak regime; however the FEM tends to significantly underestimate the ductility of the test specimens. For all 18 tests in Table 1 and Fig. 12, the proposed kinematic approach produces an average shear strength experimental-to-predicted ratio of 1.02 with a coefficient of variation (COV) of 7.4%. The respective values obtained with the FEM are 0.99 and 6.9%. It can therefore be concluded that, while the kinematic model is significantly simpler and computationally more effective with no open input parameters, it also produces virtually identical shear strength predictions to those of the complex nonlinear finite element model.

Table 1 — Tests of short FRP coupling beams[8,9]